Nano Research

Open Access

Research Article

Mining iron from stainless steel pickling wastewater to produce quasi-MIL-100(Fe) for boosted photocatalytic peroxymonosulfate activation

Miao Chang[1,2], Fei Wang[1,2], Zhaoyi Liu[1,2], Xiao-Hong Yi[1,2], Hongyu Chu[1,2], Liang Zhang[3], Xudong Zhao[4], Chong-Chen Wang[1,2] ✉, Peng Wang[1,2], and Junhu Wang[5]

[1] *Institute of Advanced Materials/Beijing Key Laboratory of Functional Materials for Building Structure and Environment Remediation, School of Environment and Energy Engineering, Beijing University of Civil Engineering and Architecture, Beijing 100044, China*
[2] *Key Laboratory of Urban Stormwater System and Water Environment (Ministry of Education), Beijing University of Civil Engineering and Architecture, Beijing 100044, China*
[3] *School of Environmental and Chemical Engineering, Jiangsu University of Science and Technology, Zhenjiang 212003, China*
[4] *College of Chemical Engineering and Technology, Taiyuan University of Science and Technology, Taiyuan 030024, China*
[5] *Center for Advanced Mössbauer Spectroscopy, Mössbauer Effect Data Center, Dalian Institute of Chemical Physics, Chinese Academy of Sciences, Dalian 116023, China*

Cite this article: *Nano Research*, **2025**, *18*, 94907382. https://doi.org/10.26599/NR.2025.94907382

ABSTRACT: Resource recovery for the preparation of high-value-added products represents a promising strategy for reducing pollution and carbon emissions. In this study, stainless steel pickling wastewater was utilized as a metal source to synthesize MIL-100(Fe), which was subsequently transformed into quasi-MIL-100(Fe) (Q350-MIL-100(Fe)) through controlled pyrolysis at an optimized temperature of 350 °C. The as-prepared Q350-MIL-100(Fe) demonstrated exceptional performance in activating peroxymonosulfate (PMS) under ultraviolet (UV) light irradiation, enabling the efficient degradation of various organic pollutants. Compared to pristine MIL-100(Fe), Q350-MIL-100(Fe) exhibited a 41.56-fold increase in the degradation rate constant for atrazine (ATZ), attributed to its narrower bandgap, abundant exposed active sites, and hierarchical porous structure. Furthermore, a self-constructed reactor employing Q350-MIL-100(Fe)/graphite felt (GF) as an immobilized catalyst achieved continuous and complete (100.0%) ATZ degradation for up to 96.0 hours. This work provides valuable insights into the sustainable utilization of industrial wastewater to produce high-value-added functional materials for environmental remediation, aligning with the dual goals of pollution control and resource recovery.

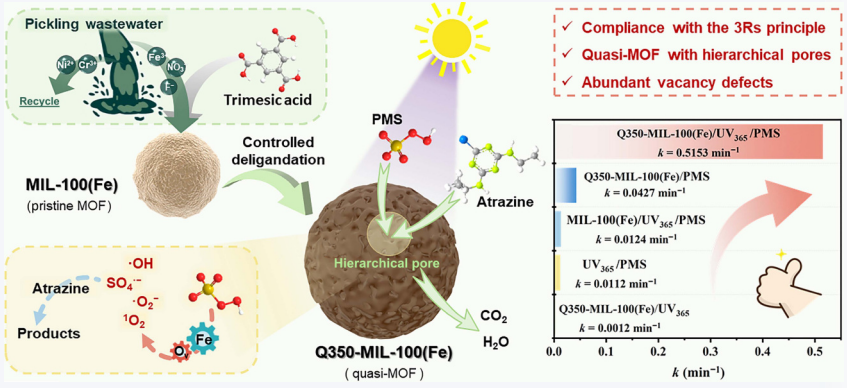

KEYWORDS: quasi-MIL-100(Fe), stainless steel pickling wastewater, resources recycling, peroxymonosulfate (PMS) activation, atrazine (ATZ) degradation

1 Introduction

Metal-organic frameworks (MOFs) have witnessed rapid development in recent years, which have been extensively studied in environmental protection, energy storage, and medicine applications [1–3]. At present, commercial metal salts are generally used as metal sources to produce MOFs, which might increase the production cost [4–6]. Using metallic wastewater to synthesize MOFs can not only reduce the cost, but also realize the harmless disposal of wastewater. Stainless steel pickling wastewater, which contains massive metal ions (like Fe^{3+}, Cr^{3+}, and Ni^{2+}), HF and HNO_3, can serve as excellent precursors to produce MOFs [7, 8].

Received: February 6, 2025; **Revised:** March 13, 2025
Accepted: March 17, 2025

✉Address correspondence to wangchongchen@bucea.edu.cn, chongchenwang@126.com

High-value-added MOFs can be synthesized by adding organic ligands to stainless steel pickling wastewater, which can solve the discharge of hazardous waste and is undoubtedly an important embodiment of the 3Rs principle (reduce, reuse, and recycle) [9, 10].

Defect engineering is an effective method of modulating energy bands, electronic structure and material properties, and the introduction of defects allows for the modulation and optimization of material properties [11, 12]. A moderate number of defects in a photocatalyst can enhance its photocatalysis activity and charge separation efficiency [13]. Conversely, an excessive number of defects will lead to a decline in charge separation efficiency. This phenomenon underscores the significance of maintaining an appropriate level of structural defects in photocatalysts [14]. Quasi-MOF, characterized by its metastable state with controlled ligand dissociation-induced defects [15], can preserve the intrinsic merits of the pristine MOFs like high specific surface area, structural versatility and tunable functionality [16]. Quasi-MOF can synergistically integrate the benefits of defect engineering to achieve superior performance to its parent MOF counterpart.

Sulfate radical-based advanced oxidation processes (SR-AOPs) is widely used for the elimination of refractory pollutants in the aquatic environment due to the high redox potential (2.5–3.1 V), long half-life time (30–40 μs) and broad operational pH adaptability (pH = 3.0–9.0) [17, 18]. These characteristics make SR-AOPs particularly effective against recalcitrant contaminants like atrazine (ATZ), an herbicide to control grassy and broadleaf weeds. The environmental persistence (half-life: 41–231 days) enables its progressive accumulation in aqueous matrices, soil ecosystems, and ultimately trophic chains through bioaccumulation processes [19, 20]. Furthermore, ATZ exhibits endocrine-disrupting characteristics and potential carcinogenicity, posing grave threats to both ecological integrity and human health. Consequently, developing efficient strategies for ATZ sequestration and degradation in aqueous environments represents an urgent priority in environmental engineering.

Inspired by the above-mentioned points, high-value-added MIL-100(Fe) was prepared economically and quickly using stainless steel pickling wastewater by relatively mild microwave method, which was used to yield quasi-MOF (Q350-MIL-100(Fe)). Atrazine, as a refractory organic contaminant, was selected to explore the photocatalytic activate peroxymonosulfate (PMS) capacity of Q350-MIL-100(Fe). In the Q350-MIL-100(Fe) construction, the skeletal structure of pristine MIL-100(Fe) was largely retained, forming a hierarchical pore structure which ensured the reactants accessibility to the exposed active sites (Fe sites and oxygen vacancies) and diffuse in a timely and effective manner. This work opened a new door to produce quasi-MOFs with appropriate defects for potential advanced oxidation processes in purification of wastewater containing emerging pollutants.

2 Experimental

2.1 Synthesis of MIL-100(Fe) with pickling wastewater

1.5 g 1,3,5-benzenetricarboxylic acid (H_3BTC) and 60.0 mL stainless steel pickling wastewater (the composition was shown in Table S1 in the Electronic Supplementary Material (ESM)) were added into a three-necked flask, which was heated to 107.0 °C in 2.5 min (750.0 W) and held on this temperature for 90.0 min in XH-100B microwave oven fitted with a set of cooling reflux device (Xianghu Co., Beijing). The as-prepared orange MIL-100(Fe) precipitates were centrifuged at 8000.0 rpm for 2.0 min and washed with ethanol for three times.

2.2 Synthesis of quasi-MOF (Q*x*-MIL-100(Fe))

The 200.0 mg MIL-100(Fe) samples were treated in tube furnace at different temperatures (250.0, 300.0, 350.0, and 400.0 °C) for 2.0 h in N_2 atmosphere with a heating rate of 5.0 °C·min^{-1}. The as-synthesized quasi-MIL-100(Fe) samples were denoted as Q*x*-MIL-100(Fe) (*x* representing the pyrolysis temperature in °C).

2.3 Catalysis experiments

Series of experiments were designed and conducted to evaluate the PMS activation ability of Q*x*-MIL-100(Fe) under ultraviolet$_{365}$ (UV_{365}) light for degrading some selected organic pollutants like atrazine (ATZ), bisphenol A (BPA), diclofenac sodium (DCF), sulfafurazole (SIZ) and rhodamine B (RhB), in which 10.0 mg of Q*x*-MIL-100(Fe) was added into 50.0 mL aqueous solution containing selected pollutants (5.0 mg·L^{-1}) in a PCX50B (Beijing Perfect Light Technology Co., Ltd, the light spectrum and intensity was shown in Fig. S1 in the ESM) reactor. Especially, after achieving adsorption equilibrium between Q*x*-MIL-100(Fe) and selected pollutant in dark for 20.0 min, 0.1 mM PMS was added into the reactor with UV_{365} light to start the reaction. During the reaction process, 1.0 mL liquor was extracted and filtered through a 0.22 μm polytetrafluoroethylene (PTFE) membrane at a specific time (0.0, 2.0, 5.0, 10.0, 15.0, 20.0, and 30.0 min), which was instantly quenched with 10.0 μL methanol. The residual pollutant concentrations were determined by liquid chromatography (LC-20A, Shimadzu, Japan). The detailed determination instruments and methods for the selected pollutants as well as the quantitative detection of different reactive oxygen species (ROSs) were listed in Table S2 in the ESM.

2.4 Continuous-flow operation tests

Graphite felt (GF) was adopted to immobilize optimal Q350-MIL-100(Fe) powder for fabricating self-designed continuous-flow reactor. In the specific coating process, 100.0 mg of Q350-MIL-100(Fe) were mixed with 0.2 mL of ethanol absolute, 0.2 mL of deionized water and 0.05 mL of PTFE emulsion to form a slurry, which was further coated onto a 25.0 mm × 60.0 mm GF, and then naturally air-dried overnight to obtain the loaded Q350-MIL-100(Fe) on the graphite felt (Q350-MIL-100(Fe)/GF).

Continuous-flow testing of ATZ degradation was performed in a self-designed reactor with 8 units. The ATZ solution with initial concentration of 5.0 mg·L^{-1} and PMS solution with the content of 250.0 mM were injected using a BT300-2J peristaltic pump (240.0 mL·h^{-1}) and a LD-P2020 flow injector (0.6 mL·h^{-1}) into the reactor containing eight GF@Q350-MIL-100(Fe) units under UV light lamp (ZLUVLAMP 85W365NM, the light spectrum and intensity was shown in Fig. S2 in the ESM), respectively, in which the hydrodynamic residence time of the treated solution in the reactor was set as 40.0 min. Then, 1.5 mL of the reaction solution was withdrawn every 60.0 min, the solution was filtered through a 0.22 μm membrane, and quenched with 10.0 μL of MeOH for further analysis.

3 Results and discussion

3.1 Characterizations

The synthesis schemes of Q350-MIL-100(Fe) and pristine MIL-

100(Fe) were shown in Fig. 1(a). The sustainable synthesis of MIL-100(Fe) was achieved through a microwave-assisted protocol utilizing stainless steel pickling wastewater as metal precursors, with only high-purity H_3BTC added as organic ligand. Compared to conventional hydrothermal synthesis requiring 24 h (19.2 kW·h in WGLL-30BE oven), the microwave method (XH-100B system) completes crystallization within 1.5 h with 1.125 kWh consumption, achieving 94.14% energy reduction. Comprehensive analysis of raw materials and energy inputs reveals 88.98% cost savings relative to commercial salt-based synthesis (Table S3 in the ESM). The process achieves dual environmental benefits by simultaneously recovering heavy metals from industrial effluent and preventing secondary pollution through wastewater detoxification.

Material characterization confirms the phase equivalency between wastewater-derived and conventional MIL-100(Fe). Powder X-ray diffraction (PXRD) patterns exhibit identical peak positions (2θ = 5°–30°) and relative intensities, confirming phase purity (Fig. S3 in the ESM). N_2 physisorption reveals comparable Brunauer–Emmett–Teller (BET) surface areas (1175.47 vs. 1200–1300 $m^2 \cdot g^{-1}$ for commercial counterparts) [21, 22].

As depicted in Fig. 1(b), the characteristic PXRD patterns of as-harvested MIL-100(Fe) corresponded well to the simulated ones from the single crystal data of CCDC: 640536, demonstrating the successful preparation of the MIL-100(Fe) [23]. As well, the characteristic PXRD peaks of both Q250-MIL-100(Fe) and Q350-MIL-100(Fe) matched well to the pristine MIL-100(Fe), with slightly weaker peak intensity. Iron oxides like Fe_3O_4 were presented in the samples obtained under the temperatures of 450.0 and 550.0 °C (Fig. S4 in the ESM), the characteristic PXRD peaks of MIL-100(Fe) disappeared. Both MIL-100(Fe) and Q350-MIL-100(Fe) exhibited rough spheroid morphology (Figs. 1(c) and 1(d)). It was obviously observed that lots of small pores were evenly distributed on the surface of Q350-MIL-100(Fe), which might be due to the missing of part ligands. The EDS element determination results revealed that C, O, and Fe without Cr were uniformly distributed over the as-prepared MIL-100(Fe) (Fig. S5 in the ESM), due to that Fe^{3+} ions were more easily coordinated to H_3BTC at relatively lower temperature than Cr^{3+} ions [9].

The characteristics of pores and composition in Q350-MIL-100(Fe) were analyzed by N_2 adsorption–desorption isotherms, thermogravimetric analysis (TGA) and CNO elemental analysis (EA). The details of the pores were presented in Table S4 in the ESM and Fig. 2(a), in which almost 38.0% more mesoporous were presented in Q350-MIL-100(Fe) than those in MIL-100(Fe). And the average pore size of Q350-MIL-100(Fe) (2.39 nm) was larger than those of MIL-100(Fe) (1.75 nm). It was found in TGA curves (Figs. 2(b) and 2(c)) that the Fe:BTC ratio in Q350-MIL-100(Fe) was 1.70, higher than that (1.55) in MIL-100(Fe) (close to Fe:BTC = 3:2 in the molecular structure), declaring that partial ligands were lost during the pyrolysis [24]. The weight loss of Q350-MIL-100(Fe) happened at 400.0 °C disappeared (Fig. S6 in the ESM), and the decrease of C, N and H element content in the EA results (Table S5 in the ESM) affirmed the loss of partial ligands.

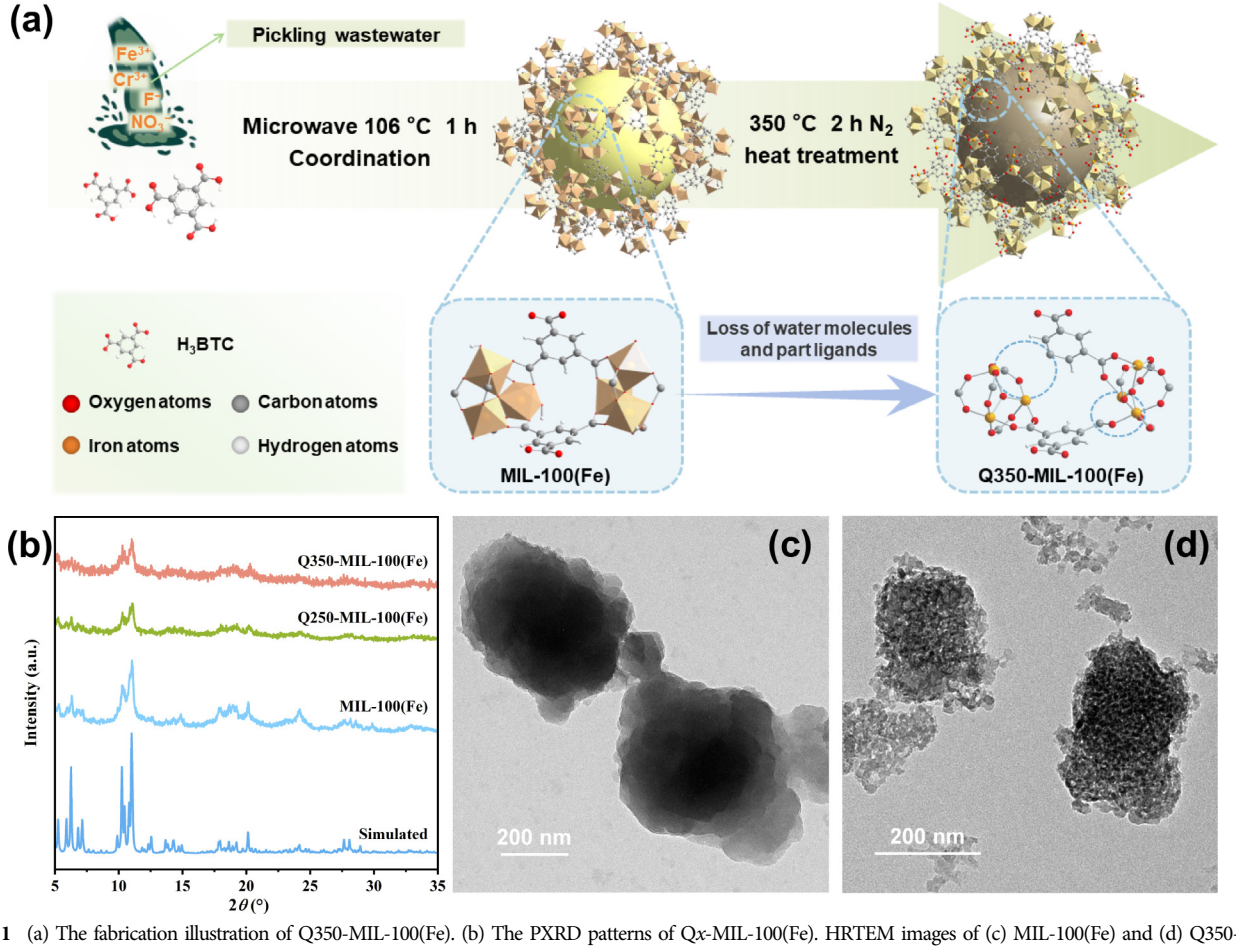

Figure 1 (a) The fabrication illustration of Q350-MIL-100(Fe). (b) The PXRD patterns of Q*x*-MIL-100(Fe). HRTEM images of (c) MIL-100(Fe) and (d) Q350-MIL-100(Fe).

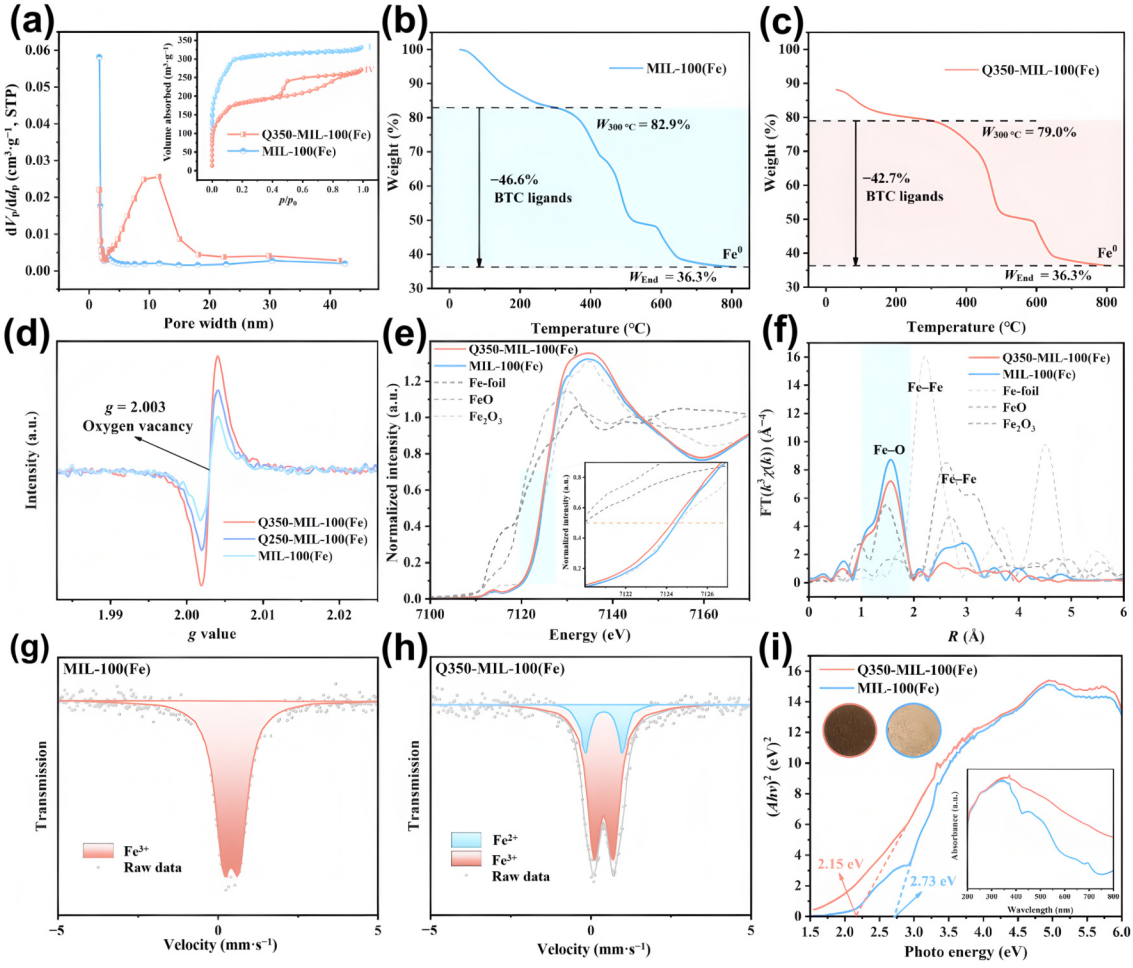

Figure 2 (a) The pore size distribution curves and the isotherms of N_2 adsorption–desorption (inset) of Q350-MIL-100(Fe) and MIL-100(Fe). TGA curves of (b) MIL-100(Fe) and (c) Q350-MIL-100(Fe). (d) The EPR spectra of Q350-MIL-100(Fe), Q250-MIL-100(Fe), and MIL-100(Fe). (e) XANES and (f) EXAFS spectra of Fe K-edge in Q350-MIL-100(Fe) and MIL-100(Fe). Room temperature ^{57}Fe Mössbauer spectra of (g) MIL-100(Fe) and (h) Q350-MIL-100(Fe). (i) The E_g plots and the UV–vis DRS spectra (inset) of Q350-MIL-100(Fe) and MIL-100(Fe).

As depicted in Fig. 2(d), the electron paramagnetic resonance (EPR) spectra of Q350-MIL-100(Fe), Q250-MIL-100(Fe) and MIL-100(Fe) displayed characteristic peaks at g = 2.003, indicating the presence of oxygen vacancies (O_v) [25], in which the O_v content in Q350-MIL-100(Fe) was higher than those in Q250-MIL-100(Fe) and MIL-100(Fe) (Table S6 in the ESM). The X-ray photoelectron spectroscopy (XPS) results shown in Fig. S7 in the ESM indicated that the peaks located at 530.89, 532.08, 533.78 eV corresponded to lattice oxygen (O_L), oxygen vacancies (O_v) along with surficial adsorbed oxygen species (O_{ad}) like O_2 and H_2O, respectively [26].

The Fe species in Q350-MIL-100(Fe) was investigated by XPS, X-ray absorption spectroscopy (XAS) and Mössbauer spectroscopy. XPS results (Fig. S8 in the ESM) showed that some Fe^{3+} ions were reduced to Fe^{2+} during pyrolysis, corresponding well with the result of X-ray absorption near edge structure (XANES) (Fig. 2(e)). The near-edge absorption of Q350-MIL-100(Fe) shifted to lower energy than that of MIL-100(Fe), and the intensity of the FT peak range in 1.0–2.0 Å decreased after pyrolysis (Fig. 2(f) and Table S7 in the ESM), implying the electron density of Fe sites of Q350-MIL-100(Fe) was enhanced [27, 28]. No obvious shift between the wavelet transformed (WT) Fe K-edge EXAFS oscillations (Fig. S9 in the ESM) of Q350-MIL-100(Fe) and MIL-100(Fe), implying that Q350-MIL-100(Fe) maintained the identical structure with MIL-100(Fe). ^{57}Fe Mössbauer spectroscopy in Figs. 2(g) and 2(h) showed that iron in MIL-100(Fe) presented one doublet, while the spectra of Q350-MIL-100(Fe) could be fitted to two symmetric doublets. In Q350-MIL-100(Fe), the doublet with large quadrupole splitting (QS) value could be attributed to the high-spin Fe^{3+} in Fe_2O_3 [29], and the smaller one could be attributed to Fe^{2+} [30], which matched well to the XPS results. And the QS value of Q350-MIL-100(Fe) was higher than MIL-100(Fe) (Table S8 in the ESM), illustrating that the asymmetry of electrons in Q350-MIL-100(Fe) was enhanced for boosted redox reaction in Q350-MIL-100(Fe) [31].

The ligand loss in quasi-MOF might influence its optical absorption properties [15]. The ultraviolet–visible diffuse reflectance spectra (UV–Vis DRS) in Fig. 2(i) showed that the light absorption ability of Q350-MIL-100(Fe) in the visible light region was improved. And the band gap (2.15 eV) of Q350-MIL-100(Fe) was lower than that (2.73 eV) of MIL-100(Fe), implying the formation of quasi-MOF could enhance the transportation of photo-induced carriers [32].

3.2 Photocatalytic PMS activation performance of Q350-MIL-100(Fe)

The photocatalytic PMS activation performances for ATZ

degradation of the different samples were evaluated under light lamps with different wavelengths (365.0, 385.0, 420.0, 450.0, 485.0, 520.0, 595.0, and 630.0 nm). It was found in Figs. S10 and S11 in the ESM that the best removal efficiency and the fastest removal rate (100.0% removal within 10.0 min) was accomplished over Q350-MIL-100(Fe) at 365.0 nm, due to that suitable high temperature (350.0 ℃) induced ideal hierarchical pores and abundant active sites [33]. It was deemed that ATZ with molecule size of 1.19 nm × 0.65 nm × 0.88 nm (Fig. S12 in the ESM) could easily enter the framework of Q350-MIL-100(Fe) with the average pore size of 2.39 nm, implying that the increasing pore size facilitates the mass transfer of ATZ molecules. The results of extended X-ray absorption fine structure (EXAFS) and Mössbauer spectra in Figs. 2(f) and 2(h) exhibited the enhancing of the asymmetry and the electron density of Fe sites in Q350-MIL-100(Fe), demonstrating that Fe species were inclined to donate electrons to promote PMS decomposition to produce different ROSs in the reaction, finally achieving Q350-MIL-100(Fe) superior oxidation ability and reaction rate [34, 35].

To confirm that the ATZ degradation resulted from the photocatalysis PMS activation process, some control experiments were carried out. The optimized dosage of PMS was fixed as 0.1 mM (Fig. S13 in the ESM). As shown in Fig. 3(a), 8.07%, 54.35%, 33.12% and 100.0% of ATZ could be degraded within 30.0 min in Q350-MIL-100(Fe)/UV_{365}, Q350-MIL-100(Fe)/PMS, UV_{365}/PMS and Q350-MIL-100(Fe)/UV_{365}/PMS systems. Pseudo-first-order kinetic ($-\ln(C/C_0) = kt$) [36] was used to calculate the reaction kinetics of ATZ degradation under different conditions. Thus, the k of Q350-MIL-100(Fe)/UV_{365}, Q350-MIL-100(Fe)/PMS, UV_{365}/PMS and Q350-MIL-100(Fe)/UV_{365}/PMS systems were evaluated as 0.0012, 0.0427, 0.0112 and 0.5153 min^{-1} (Fig. 3(b)). Thus, the synergistic index between the photocatalysis and PMS activation over Q350-MIL-100(Fe) was calculated as 11.74, demonstrating a well synergy effect [37]. In addition, the ATZ degradation efficiency of pristine MIL-100(Fe) was only 48.46% in 30.0 min with the participation of ultraviolet light and PMS. And its apparent reaction rate (k = 0.0124 min^{-1}) was 41.56 times lower than that of Q350-MIL-100(Fe) (k = 0.5153 min^{-1}), implying that defects in Q350-MIL-100(Fe) formed from partial loss of ligands resulted in superior ATZ degradation efficiency and rate.

Q350-MIL-100(Fe) exhibited satisfactory ATZ degradation efficiencies in pH range of 3.5–9.5, verifying the high tolerance to a wide pH range (Fig. S14 in the ESM). To further explore the potential of materials in practical application, Fig. 3(c) illustrated the influences of different ions (Cl^-, HCO_3^-, SO_4^{2-}, NO_3^- and $H_2PO_4^-$) on ATZ degradation, in which the corresponding concentrations referred to the surface water quality of Beijing [38]. It was observed that the ATZ degradation efficiencies were hardly affected by NO_3^-, SO_4^{2-} and $H_2PO_4^-$, while Cl^- and HCO_3^- had an inhibitory effect on the degradation process. As to Cl^-, the negative effects on ATZ degradation might be assigned to the generation of ROSs with lower redox potentials like $Cl^{\cdot}$ and $Cl_2^{\cdot-}$ [39, 40]. When 272.0 mg·L^{-1} HCO_3^- was added, the ATZ removal efficiencies decreased from 100.0% to 9.4% within 10.0 min, which might be due to the elevated pH and scavenging of ROSs by HCO_3^- [41]. To further explore the influence of HCO_3^-, some experiments were carried out at different HCO_3^- concentrations and different pH (with 272.0 mg·L^{-1} HCO_3^- addition). As displayed in Figs. S15(a) and S15(b) in the ESM, ATZ was easier to be degraded at lower pH and HCO_3^- concentrations. The results were attributed to that the added HCO_3^- mainly existed in the form of H_2CO_3 at the pH ≤ 5 (Fig. S15(c) in the ESM) and that lower HCO_3^- concentrations

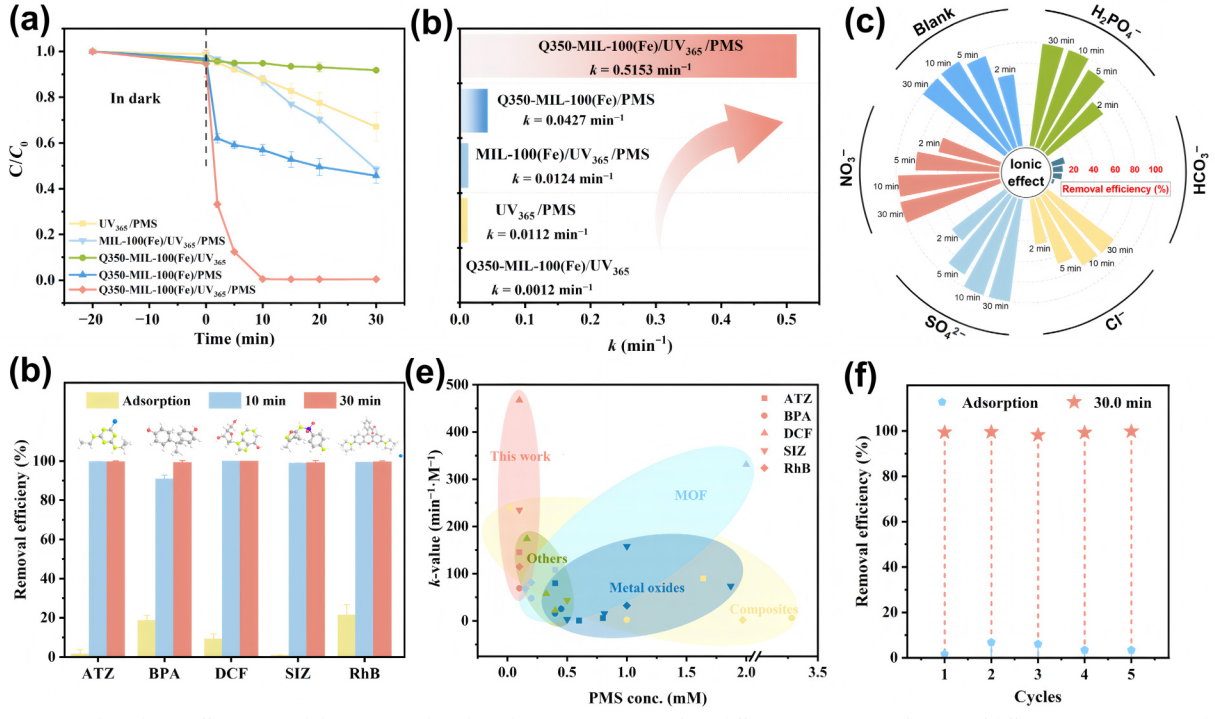

Figure 3 (a) ATZ degradation efficiencies and (b) corresponding degradation rate constants (k) in different systems. (c) Influences of different inorganic ions in the Q350-MIL-100(Fe)/UV_{365}/PMS system ($H_2PO_4^-$: 5.0 mg·L^{-1}, HCO_3^-: 272.0 mg·L^{-1}, Cl^-: 135.3 mg·L^{-1}, SO_4^{2-}: 124.0 mg·L^{-1}, and NO_3^-: 13.6 mg·L^{-1}). (d) Removal efficiencies of multiple pollutants by Q350-MIL-100(Fe). (e) Comparison of the k-value of contaminant removal in different photocatalytic activate PMS systems. (f) Cycling experiments of Q350-MIL-100(Fe)/UV_{365}/PMS system. Reaction conditions: catalysts: 0.2 g·L^{-1}, ATZ: 5 mg·L^{-1} (the concentrations of BPA, DCF, SIZ and RhB were also 5.0 mg·L^{-1}), volume = 50 mL, pH = 5.63, PMS: 0.1 mM. In different controlled variable experiments, only one factor changed.

interfered less with degradation. Besides, it was observed that the decomposition efficiency was promoted at pH = 3, which in consequence of the lower pH facilitated the degradation (Fig. S14 in the ESM) and the influence of H_2CO_3 could be neglected.

The excellent catalytic activities of Q350-MIL-100(Fe) were also found in other pollutants like BPA, DCF, SIZ and RhB (Fig. 3(d)). To eliminate the influence of reaction conditions on reaction rate constant k, k-value, a modified kinetic model, was introduced to evaluate the oxidation reaction kinetics in different heterogeneous SR-AOP systems [42]. It can be found that the k-value of Q350-MIL-100(Fe) exceeded most of the reported catalysts (Fig. 3(e) and Table S9 in the ESM). As depicted in Fig. 3(f), the degradation efficiency of Q350-MIL-100(Fe) remained almost 100.0% up to five successive cycles of experiments, demonstrating the good reusability and stability of Q350-MIL-100(Fe), which was further affirmed by the identical high-resolution transmission electron microscopy (HRTEM) images and PXRD patterns of Q350-MIL-100(Fe) before and after SR-AOP reaction (Fig. S16 in the ESM). What's more, the Fe leaching concentration of Q350-MIL-100(Fe) was measured as 1.06 mg·L^{-1} by inductively coupled plasma optical emission spectrometer (ICP-OES, ICP 5000), lower than the effluent standard of 2.0 mg·L^{-1} (DB11/307–2013). The ATZ degradation through PMS activation mediated by dissolved ferrous ions demonstrated 56.01% removal efficiency (with a rate constant k = 0.0266 min^{-1}) when Fe^{2+} was maintained at equivalent concentration levels. This observation effectively eliminated the possibility of significant contributions from homogeneous catalytic processes in the reaction system (Fig. S17 in the ESM).

3.3 Possible reaction mechanisms

In order to clarify the dominant ROSs, a series of quenching experiments and electron spin resonance (ESR) tests were carried out. Isopropanol (IPA), ethanol absolute (EtOH), ascorbic acid and $_L$-histidine were introduced as scavengers to quench ·OH, $SO_4^{\cdot-}$, $\cdot O_2^-$ and $^1O_2$ [43–47]. As shown in Fig. 4(a), the addition of IPA, EtOH, ascorbic acid and $_L$-histidine inhibited the ATZ degradation efficiencies by 73.29%, 59.76%, 73.42%, and 62.15%, respectively, indicating that all ·OH, $SO_4^{\cdot-}$, $\cdot O_2^-$ and $^1O_2$ played important roles on the ATZ degradation. The probe experiment results of BA, NBA and NBT complemented the quenching experiment (Fig. S18 in the ESM) [48, 49]. Besides, the EPR technology was used to further qualitatively distinguish the ROSs in the Q350-MIL-100(Fe) photocatalysis-activated reaction under dark and UV light. As depicted in Fig. S19 in the ESM, there was no signal in the dark, while the clear signals of 5,5-dimethyl-1-pyrroline N-oxide (DMPO)-$\cdot O_2^-$, DMPO-·OH, DMPO-$SO_4^{\cdot-}$, 2,2,6,6-tetramethyl-4-piperidone hydrochloride (TEMP)-$^1O_2$ were detected in the Q350-MIL-100(Fe)/UV_{365}/PMS system (Fig. 4(b)), further demonstrating that the photocatalysis process could boost the production of ROSs.

It was found that the $SO_4^{\cdot-}$ concentration was 18.51 μM when the molar ratio of PMS and 4-hydroxybenzoic acid (HBA) was 1:7, and the ·OH radical concentration was accumulated to 60.39 μM, when the molar ratio of PMS and benzoic acid (BA) was 1:11 [50, 51]. In order to further explain that the hierarchical pores formed after pyrolysis was beneficial to the utilization efficiency of ROSs, we also quantified $SO_4^{\cdot-}$ and ·OH in MIL-100(Fe)/UV_{365}/PMS system, and found that $SO_4^{\cdot-}$ and ·OH in this system were 4.71 and 35.36 μM, respectively, which were far less than those in Q350-MIL-100(Fe)/UV_{365}/PMS system, providing strong evidence for the hierarchical pores to effectively improve the PMS utilization (Fig.4(c) and Fig. S20 in the ESM). Pre-mixing experiments were conducted to prove this point. As presented in Fig. S21 in the ESM, the degradation of ATZ by Q350-MIL-100(Fe) showed a decreasing trend both in terms of degradation efficiency and rate with the increase of pre-mixing time. While the effect of pre-mixing time on

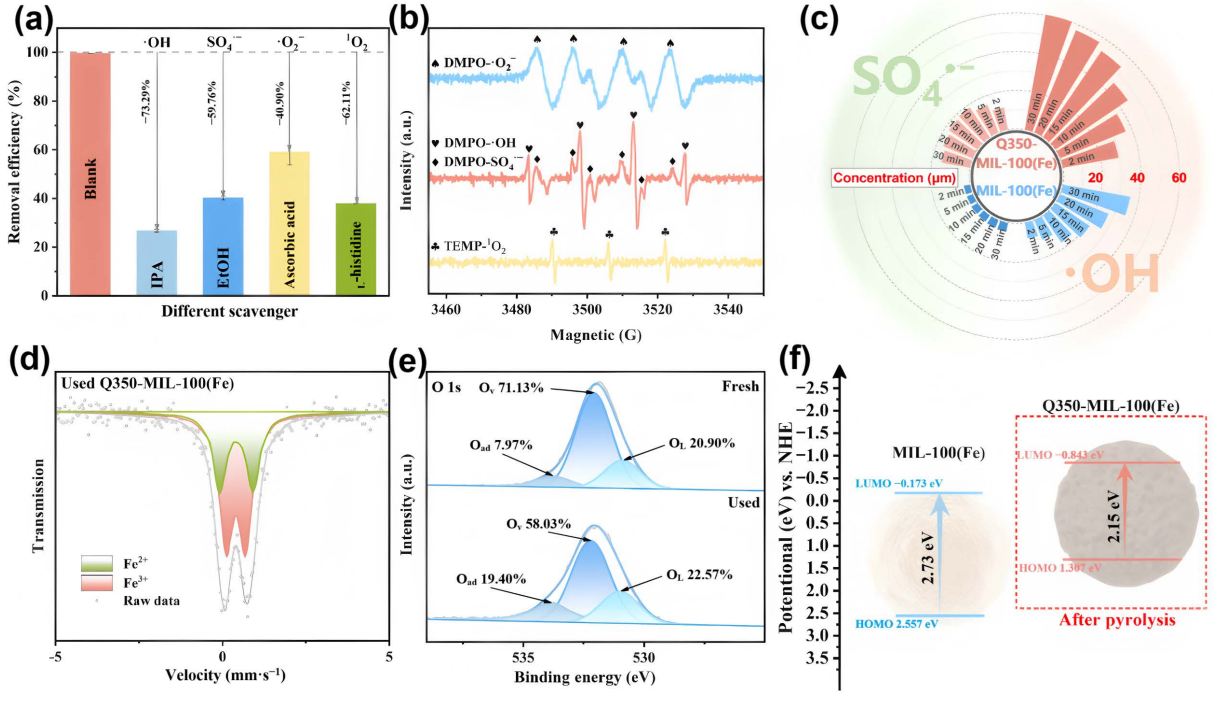

Figure 4 (a) Effects of different scavengers on ATZ degradation using Q350-MIL-100(Fe). Reaction conditions: catalysts: 0.2 g·L^{-1}, ATZ: 5 mg·L^{-1}, volume = 50 mL, pH = 5.63, PMS = 0.1 mM. (b) The ESR spectra of DMPO-$\cdot O_2^-$, DMPO-·OH, DMPO-$SO_4^{\cdot-}$, TEMP-$^1O_2$ over Q350-MIL-100(Fe)/UV_{365}/PMS. (c) Quantification of ·OH and $SO_4^{\cdot-}$ in Q350-MIL-100(Fe)/UV_{365}/PMS and MIL-100(Fe)/UV_{365}/PMS system. (d) Room temperature ^{57}Fe Mössbauer spectra of used Q350-MIL-100(Fe). (e) XPS spectra of O 1s in Q350-MIL-100(Fe) before and after photocatalytic degradation of ATZ. (f) The HOMO and LUMO position of MIL-100(Fe) and Q350-MIL-100(Fe).

the MIL-100(Fe) system was almost negligible. This also demonstrated that the hierarchical pores of Q350-MIL-100(Fe) promoted the PMS activation reaction.

The active sites for PMS activation were generally considered to be metallic sites such as Fe and non-metallic sites such as O_v. Active sites masking experiments were performed to identify the actual active sites. Ethylenediaminetetraacetic acid disodium salt (EDTA-2Na) and NaH_2PO_4 were used as Fe site masking agents to verify the active site [52, 53]. The experimental results are shown in Fig. S22 in the ESM, and it was found that the degradation process of ATZ was both inhibited to a large extent, indicating that Fe was the main reaction site. The above discussion was confirmed by the increase of Fe(II) in the XPS analysis and Mössbauer spectroscopy of the used Q350-MIL-100(Fe) (Fig. 4(d) and Fig. S23 in the ESM). In addition, O_v was masked with $Na_2S{\cdot}9H_2O$ to identify the function of oxygen vacancies [54]. As shown in Fig. S24 in the ESM, the addition of the oxygen vacancy masker inhibited 48.99% of ATZ degradation, indicating that oxygen vacancies also played an important role in the photocatalytic activation of PMS to degrade ATZ. Moreover, the reduction in the percentage of O_v content in XPS O 1s of the used Q350-MIL-100(Fe) (Fig. 4(e)), and the O_v content in Q*x*-MIL-100(Fe) was positively correlated with the apparent reaction rate (*k*) of ATZ degradation (Fig. S25 in the ESM), both confirming the important role of oxygen vacancies.

To make clear the possible photocatalysis PMS activation mechanism over Q350-MIL-100(Fe), the band positions of Q350-MIL-100(Fe) and MIL-100(Fe) were measured by UV–Vis DRS, and the HOMO and LUMO positions were obtained by combining with Mott–Schottky plots. As illustrated in Fig. S26 in the ESM, the flat band position of Q350-MIL-100(Fe) and MIL-100(Fe) were −1.04 and 0.37 eV (vs. Ag/AgCl, pH = 7.0). So, the E_{LUMO} of Q350-MIL-100(Fe) and MIL-100(Fe) were −0.843 and −0.173 eV (vs. NHE at pH = 7), the E_{HOMO} of Q350-MIL-100(Fe) and MIL-100(Fe) were 1.307 and 2.557 eV (vs. NHE at pH = 7). The HOMO and LUMO energy levels of Q350-MIL-100(Fe) evidently decreased (Fig. 4(f)), and the band gap was narrower contrasted to MIL-100(Fe), indicating that the redox capacity of Q350-MIL-100(Fe) was enhanced, promoting the activation of PMS under light [55]. Photoluminescence (PL) spectroscopy was used to test the recombination rate of photoinduced electrons and holes. As shown in Fig. S27 in the ESM, the Q350-MIL-100(Fe) could maintain longer lifetime of photo-induced charge carriers than MIL-100(Fe) [56]. Moreover, the Nyquist arc radius of Q350-MIL-100(Fe) was smaller than MIL-100(Fe) (Fig. S28 in the ESM), and the radius further decreased with the addition of ultraviolet light and PMS, suggesting the UV irradiation and PMS reduced the charge transfer resistance and the electron transfer was more likely to happen in photocatalytic activation of PMS process [57].

Combined with experiments and various characterizations, the possible mechanism of ATZ degradation in the Q350-MIL-100(Fe)/UV_{365}/PMS system could infer to be a multi-channel synergistic degradation process as demonstrated in Fig. 5: (i) the HSO_5^- activated directly by UV light to produce $SO_4^{\cdot-}$, $^1O_2$, ·OH, and $\cdot O_2^-$ in solution to degrade ATZ, which was called as direct photo-activation process; (ii) the direct electron transfer activation of PMS by photogenerated electrons could produce ROSs in solution to attack the ATZ; (iii) the photoexcited electrons facilitated the *in situ* redox cycles of Fe^{2+}/Fe^{3+} in Q350-MIL-100(Fe), accelerated the activation of PMS to generate ROSs and improved the catalytic performance, which process was called indirect electron transfer activation process; (iv) PMS acted as an electron donor and reacted with Fe^{2+}/Fe^{3+} in Q350-MIL-100(Fe), accelerated the activation of PMS to generate ROSs and improved the catalytic performance, which Q350-MIL-100(Fe) to transfer e^- to reduce Fe^{3+} to Fe^{2+} forming $SO_5^{\cdot-}$, and further formed $^1O_2$ to degrade pollutants; (v) oxygen vacancies as electron enrichment center could also facilitate the reaction.

3.4 Potential practical application of Q350-MIL-100(Fe)

Based on the excellent results of the intermittent cyclic experiments,

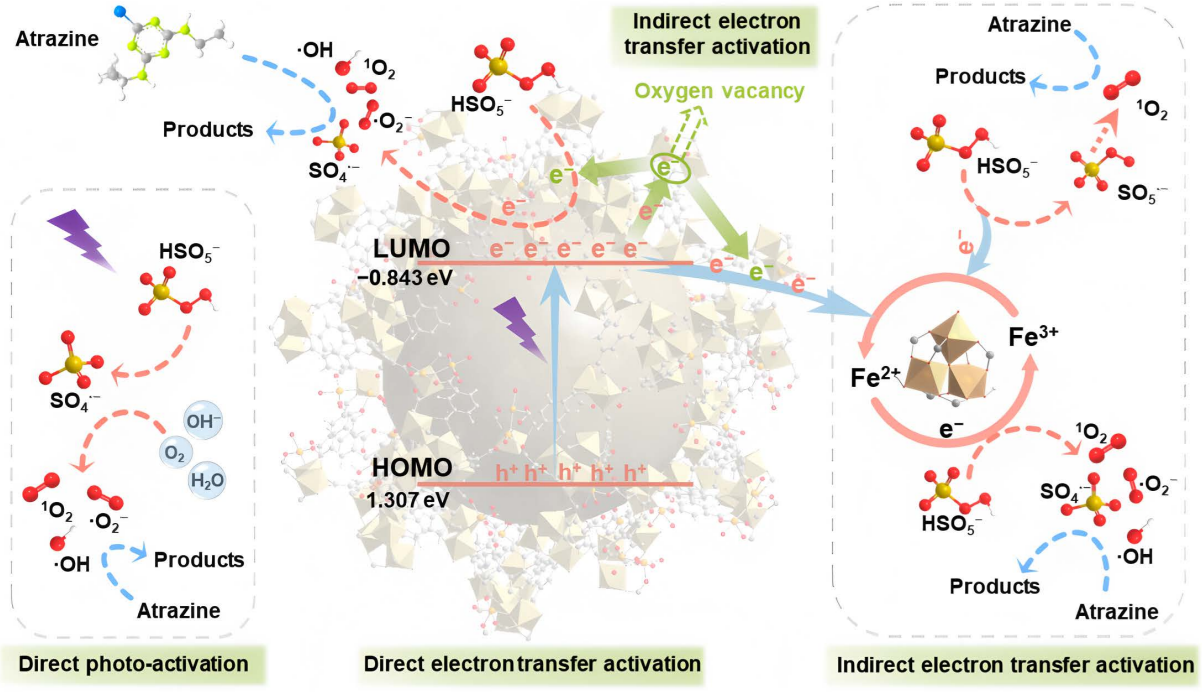

Figure 5 The plausible mechanisms of ATZ degradation in the Q350-MIL-100(Fe)/UV_{365}/PMS system.

continuous operation experiment was carried out. As the structure of GF could be beneficial to the permeation and diffusion of the contaminant solution [58], GF was selected as the catalyst carrier to support the continuous degradation experiments. Therefore, the catalyst Q350-MIL-100(Fe) was stably attached to the surface of GF with the help of PTFE, forming an immobilized Q350-MIL-100(Fe)/GF catalyst. The 365.0 nm UV light could promote the photocatalytic activation process of PMS to degrade the pollutants efficiently, so the continuous degradation experiments were carried out under 365.0 nm UV light irradiation. The continuous degradation performance of ATZ was effectively evaluated in a self-made reactor for a long time (Figs. 6(a) and 6(b)). The catalyst was loaded stably and didn't fall off before and after the reaction. As shown in Fig. 6(c), the ATZ degradation efficiency of Q350-MIL-100(Fe)/UV_{365}/PMS system could remain above 97.0% after 96.0 h of continuous operation (the amount of ATZ degraded per unit mass of catalyst was not less than 144.0 mg·g^{-1}), indicating that Q350-MIL-100(Fe)/GF has good photocatalytic activation capabilities for PMS and long-term stability. On the contrary, in the single GF/UV_{365}/PMS system, the degradation efficiency of ATZ was only about 40.0%, which showed that Q350-MIL-100(Fe) was crucial to the continuous degradation of ATZ. The average leaching concentration (1.81 mg·L^{-1}) of Fe with Q350-MIL-100(Fe)/GF during continuous flow operation was lower than the integrated discharge standard of water pollutants in Beijing, demonstrating that Q350-MIL-100(Fe) had the potential to continuously degrade refractory pollutants in water. Q350-MIL-100(Fe) was further used to activate PMS for ATZ degradation upon the real solar light. The sunlight spectrum of Daxing campus of BUCEA and the picture of device were shown in Fig. 6(d). It was observed that ATZ removal efficiency reached 100.0% within 10.0 min in the Q350-MIL-100(Fe)/Sunlight/PMS system (Fig. 6(f)), which was superior to

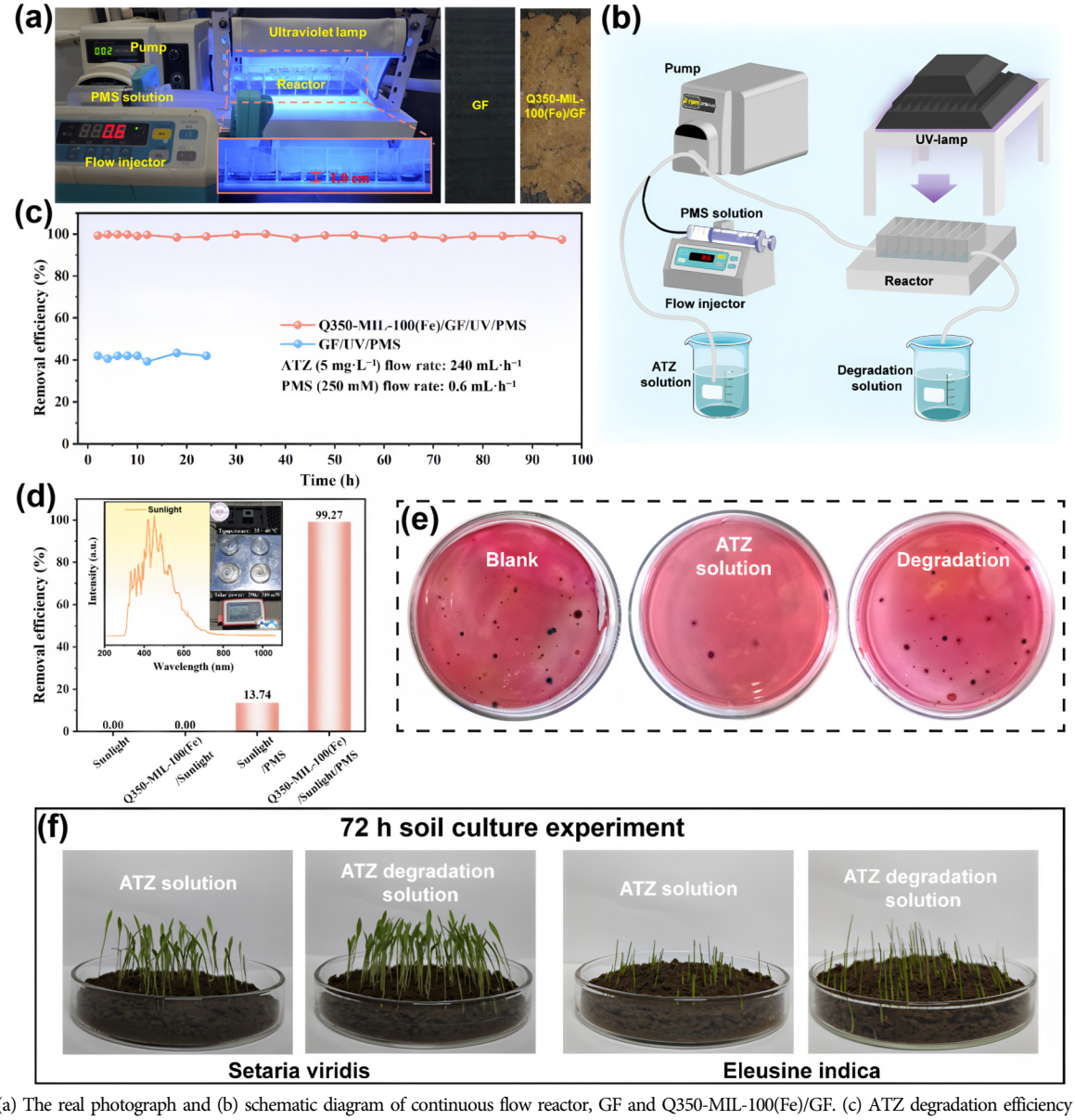

Figure 6 (a) The real photograph and (b) schematic diagram of continuous flow reactor, GF and Q350-MIL-100(Fe)/GF. (c) ATZ degradation efficiency in different continuous flow systems. (d) Degradation efficiency of ATZ under real sunlight, and the solar spectrum and real solar experimental device (inset). Reaction conditions: Q350-MIL-100(Fe) catalysts: 0.2 g·L^{-1}, ATZ: 5.0 mg·L^{-1}, volume = 50.0 mL, pH = 5.63, PMS: 0.1 mM. (e) Chromogenic agar test to observe the effect of ATZ solution on bacteria in lake water before and after degradation. (f) Growth of setaria viridis and eleusine indica under watering with ATZ solution and degradation solution after 72.0 h.

single Sunlight, Sunlight/PMS and Q350-MIL-100(Fe)/sunlight systems. The results showed that Q350-MIL-100(Fe) also had good pollutant removal ability under real sunlight.

Figure S29 in the ESM displayed three possible pathways of ATZ degradation in Q350-MIL-100(Fe)/UV_{365}/PMS system based on high-resolution mass spectrometry (HRMS) [59, 60]. And toxicity of intermediates was preliminarily assessed using Toxicity Estimation Software (T.E.S.T.) (Fig. S30 in the ESM), showing ATZ was degraded to less toxic compounds. Biotoxicity experiments, observing the growth behavior of lake water bacteria and gramineae plants, were conducted on the ATZ liquor before and after degradation to further demonstrate the low toxicity of the degradation intermediates. As shown in Fig. 6(e), the growth of lake water bacteria in the ATZ degradation solution was similar to the blank, while the growth was significantly inhibited in the ATZ solution. And the results of Gramineae plants growth were shown in Fig. 6(f) and Fig. S31 in the ESM. Although the setaria viridis could grow in ATZ solution after 72.0 h, the whole growth trend was not good, its stems were low-growing, and the leaves were yellow-like. On the contrary, after 72.0 h in ATZ degradation solution, its growth was good, the plants were denser than that in ATZ solution. The leaves were healthy and green, and its growth height was higher than that in ATZ solution. This phenomenon was more obvious in the growth of eleusine indica. The above results demonstrated the toxicity of degraded ATZ and its intermediate products was obviously reduced, and Q350-MIL-100(Fe)/UV_{365}/PMS system has good ecological safety in wastewater treatment.

4 Conclusions

High-value-added MIL-100(Fe) was prepared by recovering metal ions from waste stainless steel pickling wastewater as the metal source, and then quasi-MOF (Q350-MIL-100(Fe)) was obtained by controllable removal of ligands through pyrolysis. Q350-MIL-100(Fe) has an efficient degradation ability of ATZ through the photocatalytic activation of the PMS process (complete degradation in 10.0 min, k = 0.5153 min^{-1}), which was 41.56 times higher than the MIL-100(Fe)/UV_{365}/PMS system. The ATZ degradation by the Q350-MIL-100(Fe)/UV_{365}/PMS system was a radical-dominated process, which was facilitated by the exposure of more Fe sites and the existence of oxygen vacancies. Moreover, the continuous removal of ATZ for up to 96.0 h (100.0% degradation efficiency) was achieved in a homemade reactor, which strongly demonstrated the potential of Q350-MIL-100(Fe) for practical applications. This research offers a valuable reference for exploring resource recovery from wastewater to synthesize high-value-added functional materials. These materials can be further applied to eliminate pollutants, aligning with the goals of both pollutant reduction and carbon reduction.

Electronic Supplementary Material: Supplementary material (chemicals and analytical characterization methods, specific parameters of stainless steel pickling wastewater, comparison of MIL-100(Fe) synthesized by commercial metal salts and stainless steel pickling wastewater, controlled experiment on Q350-MIL-100(Fe)/UV/PMS system, Fe and oxygen vacancies masking experiments, the possible pathway of ATZ degradation based on HRMS and the toxicity analysis by T.E.S.T., toxicity test, etc.) is available in the online version of this article at https://doi.org/10.26599/NR.2025.94907382.

Data availability

All data needed to support the conclusions in the paper are presented in the manuscript and the ESM. Additional data related to this paper may be requested from the corresponding author upon request.

Acknowledgements

This work was supported by the National Natural Science Foundation of China (Nos. 52370025 and 22176012) and BUCEA Post Graduate Innovation Project (No. PG2024086).

Declaration of competing interest

All the contributing authors report no conflict of interests in this work.

Author contribution statement

M. C.: Conceptualization, data curation, formal analysis, investigation, methodology, validation, visualization, writing – original draft. F. W.: Data curation, methodology. Z. Y. L.: Data curation. X.-H. Y.: Investigation, methodology. H. Y. C.: Visualization, methodology. L. Z.: Methodology. X. D. Z.: Resources. C.-C. W.: Conceptualization, funding acquisition, project administration, resources, supervision, writing – review & editing. P. W.: Resources. J. H. W.: Resources, methodology.

Use of AI statement

None.

References

[1] Ding, M. L.; Cai, X. C.; Jiang, H. L. Improving MOF stability: Approaches and applications. *Chem. Sci.* **2019**, *10*, 10209–10230.

[2] Chu, H. Y.; Wang, C. C. MIL-100(Fe)-based functional materials for water decontamination: A state of the art review. *Prog. Natur. Sci. Mater. Int.* **2023**, *33*, 386–406.

[3] Yi, X. H.; Wang, C. C. Metal-organic frameworks on 3D interconnected macroporous sponge foams for large-scale water decontamination: A mini review. *Chin. Chem. Lett.* **2024**, *35*, 109094.

[4] Rubio-Martinez, M.; Avci-Camur, C.; Thornton, A. W.; Imaz, I.; Maspoch, D.; Hill, M. R. New synthetic routes towards MOF production at scale. *Chem. Soc. Rev.* **2017**, *46*, 3453–3480.

[5] Julien, P. A.; Mottillo, C.; Friščić, T. Metal-organic frameworks meet scalable and sustainable synthesis. *Green Chem.* **2017**, *19*, 2729–2747.

[6] Kong, X. J.; Li, J. R. An overview of metal-organic frameworks for green chemical engineering. *Engineering* **2021**, *7*, 1115–1139.

[7] Rögener, F.; Sartor, M.; Bán, A.; Buchloh, D.; Reichardt, T. Metal recovery from spent stainless steel pickling solutions. *Resour., Conserv. Recycl.* **2012**, *60*, 72–77.

[8] Wu, M. T.; Li, Y. L.; Guo, Q.; Shao, D. W.; He, M. M.; Qi, T. Harmless treatment and resource utilization of stainless steel pickling sludge via direct reduction and magnetic separation. *J. Cleaner Prod.* **2019**, *240*, 118187.

[9] Zhao, X. D.; Zhang, C. W.; Liu, B. S.; Zhao, H. F.; Gao, X. L.; Wang, Y. Y.; Zhang, Y. Z.; Liu, D. H.; Wang, C. C. Resource mining from stainless steel pickling wastewater to produce metal-organic frameworks. *Resour., Conserv. Recycl.* **2023**, *188*, 106647.

[10] Zhao, X. D.; Zhang, L. S.; Liu, B. S.; Zhang, C. W.; Zhao, H. F.; Wang, C. C.; Liu, D. H. Recycling of stainless steel pickling

wastewater and polyethylene terephthalate plastic: A total-waste synthesis of metal-organic framework. *Prog. Natur. Sci. Mater. Int.* **2023**, *33*, 478–485.

[11] Fang, Z. L.; Bueken, B.; De Vos, D. E.; Fischer, R. A. Defect-engineered metal-organic frameworks. *Angew. Chem., Int. Ed.* **2015**, *54*, 7234–7254.

[12] Li, Y. H.; Wang, P.; Wang, C. C.; Liu, Y. B. State-of-the-art review of defective metal-organic frameworks for pollutant removal from water. *Chin. J. Inorg. Chem.* **2022**, *38*, 2342–2362.

[13] Wang, J.; Duan, X. G.; Gao, J.; Shen, Y.; Feng, X. H.; Yu, Z. J.; Tan, X. Y.; Liu, S. M.; Wang, S. B. Roles of structure defect, oxygen groups and heteroatom doping on carbon in nonradical oxidation of water contaminants. *Water Res.* **2020**, *185*, 116244.

[14] Ma, X.; Wang, L.; Zhang, Q.; Jiang, H. L. Switching on the photocatalysis of metal-organic frameworks by engineering structural defects. *Angew. Chem., Int. Ed.* **2019**, *58*, 12175–12179.

[15] Bagheri, M.; Masoomi, M. Y. Quasi-metal organic frameworks: Preparation, applications and future perspectives. *Coord. Chem. Rev.* **2022**, *468*, 214643.

[16] Tsumori, N.; Chen, L. Y.; Wang, Q. J.; Zhu, Q. L.; Kitta, M.; Xu, Q. Quasi-MOF: Exposing inorganic nodes to guest metal nanoparticles for drastically enhanced catalytic activity. *Chem* **2018**, *4*, 845–856.

[17] Wang, J. L.; Wang, S. Z. Activation of persulfate (PS) and peroxymonosulfate (PMS) and application for the degradation of emerging contaminants. *Chem. Eng. J.* **2018**, *334*, 1502–1517.

[18] Yi, X. H.; Ji, H. D.; Wang, C. C.; Li, Y.; Li, Y. H.; Zhao, C.; Wang, A.; Fu, H. F.; Wang, P.; Zhao, X. et al. Photocatalysis-activated SR-AOP over PDINH/MIL-88A(Fe) composites for boosted chloroquine phosphate degradation: Performance, mechanism, pathway and DFT calculations. *Appl. Catal. B: Environ.* **2021**, *293*, 120229.

[19] Singh, S.; Kumar, V.; Chauhan, A.; Datta, S.; Wani, A. B.; Singh, N.; Singh, J. Toxicity, degradation and analysis of the herbicide atrazine. *Environ. Chem. Lett.* **2018**, *16*, 211–237.

[20] Li, J.; Yan, J. F.; Yao, G.; Zhang, Y. H.; Li, X.; Lai, B. Improving the degradation of atrazine in the three-dimensional (3D) electrochemical process using $CuFe_2O_4$ as both particle electrode and catalyst for persulfate activation. *Chem. Eng. J.* **2019**, *361*, 1317–1332.

[21] Chang, M.; Tang, C. Y.; Wang, C. C.; Zhao, C. From ore to MOF: A case of MIL-100(Fe) production from iron ore concentrates. *Prog. Natur. Sci. Mater. Int.* **2024**, *34*, 66–73.

[22] Wang, J. W.; Qiu, F. G.; Wang, P.; Ge, C. J.; Wang, C. C. Boosted bisphenol A and Cr(VI) cleanup over Z-scheme WO_3/MIL-100(Fe) composites under visible light. *J. Cleaner Prod.* **2021**, *279*, 123408.

[23] Horcajada, P.; Surblé, S.; Serre, C.; Hong, D. Y.; Seo, Y. K.; Chang, J. S.; Grenèche, J. M.; Margiolaki, I.; Férey, G. Synthesis and catalytic properties of MIL-100(Fe), an iron(III) carboxylate with large pores. *Chem. Commun*. **2007**, 2820–2822.

[24] Huangfu, C. Y.; Yu, S. N.; Tong, B.; Yang, A. N.; Lyu, J. F.; Guo, X. H. Efficient lithium extraction from aqueous solutions by MIL-100 (Fe): A study on adsorption kinetics, thermodynamics and mechanism. *Sep. Purif. Technol.* **2023**, *322*, 124365.

[25] Sun, H. Z.; Song, G.; Gong, W. B.; Lu, W. B.; Cong, S.; Zhao, Z. G. Stabilizing photo-induced vacancy defects in MOF matrix for high-performance SERS detection. *Nano Res.* **2022**, *15*, 5347–5354.

[26] Zhao, J. J.; Li, F. C.; Wei, H. X.; Ai, H. N.; Gu, L.; Chen, J.; Zhang, L.; Chi, M. H.; Zhai, J. Superior performance of $ZnCoO_x$/peroxymonosulfate system for organic pollutants removal by enhancing singlet oxygen generation: The effect of oxygen vacancies. *Chem. Eng. J.* **2021**, *409*, 128150.

[27] Huang, H. J.; Yu, D. S.; Hu, F.; Huang, S. C.; Song, J. N.; Chen, H. Y.; Li, L. L.; Peng, S. J. Clusters induced electron redistribution to tune oxygen reduction activity of transition metal single-atom for metal-air batteries. *Angew. Chem.* **2022**, *134*, e202116068.

[28] Zhao, S. L.; Wang, Y.; Dong, J. C.; He, C. T.; Yin, H. J.; An, P. F.; Zhao, K.; Zhang, X. F.; Gao, C.; Zhang, L. J. et al. Ultrathin metal-organic framework nanosheets for electrocatalytic oxygen evolution. *Nat. Energy* **2016**, *1*, 16184.

[29] Zhang, L.; Zhang, B. F.; Liu, Y. X.; Wang, Z. N.; Shah, J. H.; Ge, R. L.; Zhou, W. H.; Kubuki, S.; Wang, J. H. Modulation of reaction pathway of Prussian blue analogues derived Zn–Fe double oxides towards organic pollutants oxidation. *Chem. Eng. J.* **2023**, *454*, 140103.

[30] Dhakshinamoorthy, A.; Alvaro, M.; Horcajada, P.; Gibson, E.; Vishnuvarthan, M.; Vimont, A.; Grenèche, J. M.; Serre, C.; Daturi, M.; Garcia, H. Comparison of porous iron trimesates basolite F300 and MIL-100 (Fe) as heterogeneous catalysts for lewis acid and oxidation reactions: Roles of structural defects and stability. *ACS Catal.* **2012**, *2*, 2060–2065.

[31] Tian, M.; Wang, X. D.; Zhu, Y. Y.; Wang, J. H.; Zhang, T. Influence of chemical states of Fe and Mn on N_2O decomposition over $LaFe_xMn_yAl_{12-x-y}O_{19}$ catalysts. *Chin. J. Catal.* **2010**, *31*, 100–105.

[32] Liu, X. S.; Zhao, X. Y.; Meng, H.; Jin, J. S. Dual MOFs composites: MIL-53 coated with amorphous UiO-66 for enhanced photocatalytic oxidation of tetracycline and methylene blue. *Nano Res.* **2023**, *16*, 6160–6166.

[33] Shang, Q. G.; Liu, Y. Y.; You, Q. L.; Yan, Y.; Yang, X. F.; Liao, G. Y.; Wang, D. S. Introduction of mesopores effectively enhances the accessibility of volatile organic compounds within the micropores of covalent triazine frameworks. *Chem. Eng. J.* **2024**, *500*, 156623.

[34] Tofoni, A.; Tavani, F.; Vandone, M.; Braglia, L.; Borfecchia, E.; Ghigna, P.; Stoian, D. C.; Grell, T.; Stolfi, S.; Colombo, V. et al. Full spectroscopic characterization of the molecular oxygen-based methane to methanol conversion over open Fe (II) sites in a metal-organic framework. *J. Am. Chem. Soc.* **2023**, *145*, 21040–21052.

[35] Wang, F.; Gao, Y.; Chai, Y. T.; Wang, C. C.; Wang, J. F.; Yi, X. H.; Li, Y.; Fu, H. F.; Zhao, C.; Wang, P. Interfacial engineering regulating electronic structure of homologous S-scheme Co_3O_4@C–TiO_2 heterojunction for enhanced Fenton-like reaction activity. *Appl. Catal. B: Environ.* **2025**, *364*, 124848.

[36] Cui, C.; Zhang, M.; Yao, X. T.; Tu, S. Q.; Hou, Z.; Jie En, V. S.; Xiang, X. Q.; Lin, J.; Cai, T.; Shen, N. et al. Dose selection of chloroquine phosphate for treatment of COVID-19 based on a physiologically based pharmacokinetic model. *Acta Pharm. Sin. B* **2020**, *10*, 1216–1227.

[37] Bai, Z. X.; Xie, Y. W.; Wei, X. C.; Zhou, L. Q.; Bao, J. Y.; Tang, R. S.; Wen, Y. X.; Zhao, Z. X.; Deng, J. G.; Zhao, Z. X. Intrinsic metal ion dual-regulated fabrication of multifunctional nano-interfacial $BiFeVO_4$/Fe-MOF for high photo-Fenton-like synergistic catalytic oxytetracycline removal. *Appl. Catal. B: Environ.* **2025**, *361*, 124634.

[38] Bai, L.; Bai, Y. J.; Hou, Y.; Zhang, S. R.; Wang, S. R.; Ding, A. Z. Ecological water replenishment to the Yongding River, China: Effects of different water sources on inorganic ions and organic matter characteristics. *Environ. Sci. Pollut. Res.* **2023**, *30*, 39107–39120.

[39] Ye, B.; Liu, Z. Y.; Zhu, X. Q.; Wu, H. J.; Liang, Z. F.; Wang, W. L.; Wu, Q. Y.; Hu, H. Y.; Zhang, X. H. Degradation of atrazine (ATZ) by ammonia/chlorine synergistic oxidation process. *Chem. Eng. J.* **2021**, *415*, 128841.

[40] Wang, J. L.; Wang, S. Z. Effect of inorganic anions on the performance of advanced oxidation processes for degradation of organic contaminants. *Chem. Eng. J.* **2021**, *411*, 128392.

[41] Li, J.; Xu, M. J.; Yao, G.; Lai, B. Enhancement of the degradation of atrazine through $CoFe_2O_4$ activated peroxymonosulfate (PMS) process: Kinetic, degradation intermediates, and toxicity evaluation. *Chem. Eng. J.* **2018**, *348*, 1012–1024.

[42] Wang, B. Q.; Cheng, C.; Jin, M. M.; He, J.; Zhang, H.; Ren, W.; Li, J.; Wang, D. S.; Li, Y. D. A site distance effect induced by reactant molecule matchup in single-atom catalysts for Fenton-like reactions. *Angew. Chem.* **2022**, *134*, e202207268.

[43] Feng, Y.; Lee, P. H.; Wu, D. L.; Shih, K. Surface-bound sulfate radical-dominated degradation of 1,4-dioxane by alumina-supported palladium (Pd/Al_2O_3) catalyzed peroxymonosulfate. *Water Res.* **2017**,

120, 12–21.

[44] Zhang, Z. C.; Wang, F. X.; Wang, F.; Wang, C. C.; Wang, P. Efficient atrazine degradation via photoactivated SR-AOP over S-BUC-21 (Fe): The formation and contribution of different reactive oxygen species. *Sep. Purif. Technol.* **2023**, *307*, 122864.

[45] Yi, X. H.; Gao, Y.; Wang, C. C.; Li, Y. H.; Chu, H. Y.; Wang, P. Photocatalytic Cr(VI) reduction over MIL-88A(Fe) on polyurethane sponge: From batch to continuous-flow operation. *Chin. Chem. Lett.* **2023**, *34*, 108029.

[46] Guo, X.; Song, L. R.; Wang, W. Y.; Li, F. F.; Ha, M. N.; Tang, J.; Ling, Q.; Cui, P.; Ke, Q. P. Visible light promoted aerobic selective photo-oxidation of cyclohexene on $LaCo_xCu_{1-x}O_3$ catalyst. *Nano Res.* **2024**, *17*, 6940–6950.

[47] Zheng, W. T.; Liu, Y. B.; Liu, W.; Ji, H. D.; Li, F.; Shen, C. S.; Fang, X. F.; Li, X.; Duan, X. G. A novel electrocatalytic filtration system with carbon nanotube supported nanoscale zerovalent copper toward ultrafast oxidation of organic pollutants. *Water Res.* **2021**, *194*, 116961.

[48] Lei, Y.; Yu, Y. F.; Lei, X.; Liang, X.; Cheng, S. S.; Ouyang, G. F.; Yang, X. Assessing the use of probes and quenchers for understanding the reactive species in advanced oxidation processes. *Environ. Sci. Technol.* **2023**, *57*, 5433–5444.

[49] Yang, M. X.; Hou, Z. X.; Zhang, X.; Gao, B. Y.; Li, Y. W.; Shang, Y. N.; Yue, Q. Y.; Duan, X. G.; Xu, X. Unveiling the origins of selective oxidation in single-atom catalysis via $Co–N_4–C$ intensified radical and nonradical pathways. *Environ. Sci. Technol.* **2022**, *56*, 11635–11645.

[50] Hwang, J. Y.; Moon, G. H.; Kim, B.; Tachikawa, T.; Majima, T.; Hong, S.; Cho, K.; Kim, W.; Choi, W. Crystal phase-dependent generation of mobile OH radicals on TiO_2: Revisiting the photocatalytic oxidation mechanism of anatase and rutile. *Appl. Catal. B: Environ.* **2021**, *286*, 119905.

[51] Hong, W. J.; Zou, J. M.; Zhao, M. Z.; Yan, S. W.; Song, W. H. Development of a five-chemical-probe method to determine multiple radicals simultaneously in hydroxyl and sulfate radical-mediated advanced oxidation processes. *Environ. Sci. Technol.* **2024**, *58*, 5616–5626.

[52] Chen, J. B.; Zhou, X. F.; Sun, P. Z.; Zhang, Y. L.; Huang, C. H. Complexation enhances Cu(II)-activated peroxydisulfate: A novel activation mechanism and Cu(III) contribution. *Environ. Sci. Technol.* **2019**, *53*, 11774–11782.

[53] Yu, D. Y.; Li, L. B.; Wu, M. H.; Crittenden, J. C. Enhanced photocatalytic ozonation of organic pollutants using an iron-based metal-organic framework. *Appl. Catal. B: Environ.* **2019**, *251*, 66–75.

[54] Liu, S. S.; Fu, H. F.; Wang, F.; Wei, Y. W.; Meng, B. X.; Wang, P.; Zhao, C.; Liu, W.; Wang, C. C. Insight into the extremely different catalytic behaviors of asymmetric and symmetric oxygen vacancies for peroxymonosulfate activation. *Appl. Catal. B: Environ.* **2024**, *346*, 123753.

[55] Zhang, Z. Z.; Dong, H. L.; Cao, Q.; Chu, S.; Zhang, H. Y. Photocatalytic activation of peroxymonosulfate by Ti-oxo clusters grafted carbon nitride: Enhanced charge transfer and bisphenol A degradation efficiency. *Chem. Eng. J.* **2024**, *497*, 154921.

[56] Jiang, H. L.; Wang, Q.; Chen, P. H.; Zheng, H. T.; Shi, J. W.; Shu, H. Y.; Liu, Y. B. Photocatalytic degradation of tetracycline by using a regenerable (Bi)BiOBr/rGO composite. *J. Cleaner Prod.* **2022**, *339*, 130771.

[57] Tang, C. Y.; Wang, C. C.; Yi, X. H.; Chang, M.; Wang, F.; Li, Y.; Wang, P. The enhanced photocatalytic peroxymonosulfate activation for 2,4-dichlorophenoxyacetic acid degradation over Z-scheme PTCDA/MIL-88A(Fe) under visible light. *Chem. Eng. J.* **2024**, *493*, 152668.

[58] Xu, Z. X.; Duong-Viet, C.; Liu, Y. F.; Baaziz, W.; Li, B.; Nguyen-Dinh, L.; Ersen, O.; Pham-Huu, C. Macroscopic graphite felt containing palladium catalyst for liquid-phase hydrogenation of cinnamaldehyde. *Appl. Catal. B: Environ.* **2019**, *244*, 128–139.

[59] Hong, Y. C.; Peng, J. L.; Zhao, X. G.; Yan, Y.; Lai, B.; Yao, G. Efficient degradation of atrazine by CoMgAl layered double oxides catalyzed peroxymonosulfate: Optimization, degradation pathways and mechanism. *Chem. Eng. J.* **2019**, *370*, 354–363.

[60] Li, J.; Wan, Y. J.; Li, Y. J.; Yao, G.; Lai, B. Surface Fe (III)/Fe (II) cycle promoted the degradation of atrazine by peroxymonosulfate activation in the presence of hydroxylamine. *Appl. Catal. B: Environ.* **2019**, *256*, 117782.